Supplementary Information

Magnetoelectric coupling drives ultrafast-charging MoS_2 anodes for sodium-ion batteries

Zhenwei Li[a], Zhiyu Zou[b], Hengyuan Hu[b], Jie Chen[a], Mengchuang Liu[a], Ping Liu[a], Wenhua Zhang[a], Chang Lu[a], Zhaoxin Meng[a], Yongqiang Ji[a], Jie Yu[c], Meisheng Han[b]*, and Yuliang Cao[a, d]*

[a]Institute of Physics, Henan Academy of Sciences, Zhengzhou 450046, China

[b]Department of Mechanical and Energy Engineering, Southern University of Science and Technology, Shenzhen 518055, China

[c]Shenzhen Engineering Lab for Supercapacitor Materials, Guangdong Provincial Key Laboratory of Semiconductor Optoelectronic Materials and Intelligent Photonic Systems, School of Material Science and Engineering, Harbin Institute of Technology, Shenzhen, University Town, Shenzhen 518055, China

[d]College of Chemistry and Molecular Sciences, Hubei Key Laboratory of Electrochemical Power Sources, Wuhan University, Wuhan, 430072, China

*Corresponding Author.

E-mail address: hanms@sustech.edu.cn; ylcao@whu.edu.cn

Experimental Section

All chemicals (Macklin Co., Ltd) were analytically pure and used as received.

Synthesis of MoS_2, MoS_2@C, and $CoMoS_2$@C: For the preparation of samples, the distinct amount of cobalt iso-octoate ($(C_{11}H_7O_2)_2Co$) /$(NH_4)_2MoS_4$/DMF (0/1.5/0, MoS_2; 0/0.6/0.9 g, MoS_2@C; 0.5/0.5/0.5 g, $CoMoS_2$@C) were added in the self-made vessels. After that, these vessels were sealed in an Ar-filled glove box, subsequently transferred to a tube furnace, heated to 550 ℃ for 10 min at a ramp rate of 10 ℃ min^{-1} in an Ar flow, and then cooled to ambient temperature naturally to obtain these samples.

Material characterizations:

The morphologies of all samples were characterized by SEM (Hitachi SU-8230). TEM equipped with EDS was performed using a Talos instrument with an acceleration voltage of 300 kV. XPS (Thermo Fisher ESCALAB Xi^+) was acquired with Al Kα (hυ = 1486.8 eV) as the excitation source. Raman spectra were tested on a Horiba Labram HR Evolution using a 532 nm laser. XRD (D/max-2500/PC, Rigaku) was used to test the crystal structure. TGA was tested in oxygen atmosphere using the Pyris I, PerkinElmer instrument over the temperature range of room temperature to 700 °C with a heating rate of 10 °C min^{-1}. Brunauer-Emmett-Teller (BET) surface areas were calculated from nitrogen sorption/desorption isotherms obtained at 77 K on an ASAP 2020 PLUS HD88 instrument. The EPR spectra were obtained using a Bruker EMXplus spectrometer. The magnetic susceptibility curves were obtained using an MPMS SQUID magnetometer over a temperature range of 2-300 K, with a sampling interval of approximately 3 K.

In-situ TEM Experiment

In situ TEM experiments were carried out on JEOL 2010F microscope working at 200 kV with a PicoFemto double-tilt TEM-STM holder provided by ZepTools Technology Company. The metallic Na, Na_2O, and $CoMoS_2$@C served as the counter electrode, electrolyte, and working electrode, respectively. $CoMoS_2$@C was adhered on a TEM Cu half-grid by electrostatic adsorption, and metallic Na was scratched by an electrochemically etched tungsten tip in a glovebox. Then, the TEM grid and the tungsten tip with metal Na were loaded onto the TEM holder and sealed in a full argon-filled bag. Before putting the tungsten tip into TEM system, it was exposured in air about 5 s to obtain Na_2O on surface of Na. In TEM, the W tip and Cu-grid were connected to the positive and negative poles of the potentiostat, respectively. Piezo-driven nanomanipulator was used to manipulate the tungsten tip with Na_2O/Na to contact the free end of the selected $CoMoS_2$@C. Once they were contacted, a constant voltage of 3 V was applied on the Na electrode with respect to $CoMoS_2$@C electrode. During the sodiation process, TEM images, SAED patterns, and movie were recorded.

In-situ Magnetometry Experiment

The magnetometry test devices were assembled using flexible packaging batteries in an argon-filled glovebox at room temperature. Operando magnetometry experiments were conducted using a Quantum Design superconducting quantum interference device at 25 ºC. Magnetic measurements were consistently performed at an applied magnetic field of 3 T, oriented parallel to the surface of the copper foil. The *in-situ* magnetic measurements were performed using an external cyclic voltammetry (CV) mode with a scan rate of 0.5 mV s^{-1}. To extract the relevant magnetic data, linear magnetic background signals originating from other components of the cell assembly were meticulously subtracted from the total magnetic moment. Specifically, a blank cell containing all components except the active material was first measured under the same *in-situ* conditions. Subsequently, an identical measurement was

performed on a cell containing the active materials. The background signal obtained from the blank cell was subtracted from the data of the cell containing the active material, and the final *in-situ* magnetic data were normalized according to the content of the target species.

Electrochemical measurements of half cells

The working electrodes were prepared by mixing 80 wt% of active materials, 10 wt% of acetylene black, and 10 wt% of polyvinylidene fluoride (PVDF) into N-methyl pyrrolidone under mechanical stirring to to make the slurries. The as-prepared slurries were uniformly coated on the copper foil, and dried at 100 ℃ under vacuum for 12 h. 2032 coin-type cells contain working electrode, counter/reference electrode (sodium foil), and separator (Whatman glass fiber), as well as electrolyte (1 M $NaPF_6$ dissloved in diglyme), which were assembled in an argon-filled glove box. The mass loading of active materials in each electrode slice is 1.1-1.3 mg cm^{-2}. Land CT2001A battery-test system (Wuhan Land Electronic co., China) was applied to evaluate the electrochemical performances of cells at the charge/discharge current densities of 0.1-20 A g^{-1} between 0.01 and 3 V. A CHI 760D electrochemical workstation (Shanghai CH Instruments Co., China) was utilized to measure CV and electrochemical impedance spectroscopy (EIS). CV measurements were performed at scanning rates of 0.1-1 mV s^{-1} from 0.01 to 3 V and from 0.01 to 1 V (vs. Na/Na^+). EIS was carried out from 10^5 to 10^{-2} Hz with an amplitude of 5 mV.

Pouch full cells preparation

For the pouch full cells assembly, the $CoMoS_2$@C and $Na_3V_2(PO_4)_3$ electrodes were used as anode and cathode, respectively. The active mass loadings of the $CoMoS_2$@C and $Na_3V_2(PO_4)_3$ electrode were set to 1.65 and 10.5 mg cm^{-2} to keep an N/P ratio of about 1.1. The separator is Celgard 2400. Prior to full-cell assembly, the $CoMoS_2$@C anode was pre-sodiated using sodium metal powder to compensate for the

initial irreversible capacity loss [1]. After removal of residual Na, the pre-sodiated $CoMoS_2$@C anode was immediately used for full-cell assembly. Both electrodes have undergone a calendering process. The prepared cathode and anode electrodes are trimmed to dimensions suitable for pouch cell assembly, with the cathode and anode alternately stacked in a total of 40 layers. The final pre-sealing of the completed pouch cell, following the filling of the electrolyte, was carried out inside a glovebox. The capacity of the assembled pouch full cell is about 1.2 Ah. The dimension of the pouch full cells is about 52.0 mm*50.0 mm*4.0 mm. The cycling and rate tests of the full cell were carried out at 0.1-3 C (1 C = 110 mA g^{-1} based on the cathode material) between 0.5-3.5 V.

Gravimetric energy density calculation

The gravimetric energy density can be obtained according to the following equation.

Gravimetric energy density (Wh kg^{-1}) $=\left(\frac{Cc\times V}{(m_{active})}\right)$

Where V, C_c, and m_{active} represent the nominal voltage (~2.08 V), cell capacity (1.2 Ah), and active mass (cathode and anode, 12.64 g), respectively.

Calculation of anode utilization in $CoMoS_2$@C‖$Na_3V_2(PO_4)_3$ pouch full cell

The utilization of the anode active material (U_n) in the full cell is defined as the fraction of its theoretical capacity that is effectively accessed during full-cell operation. It can be calculated using the following procedure:

1. Theoretical anode capacity

The total theoretical capacity of the anode is given by:

$$C_{n,theo} = m_n \times s_n$$

Where m_n is the mass of the anode active material (1.79 g), and s_n is the reversible specific capacity of the anode measured in a half-cell (764.0 mAh g^{-1}).

2. Full-cell discharge capacity

The full-cell discharge capacity Q_{cell} (1200 mAh) is directly obtained from the galvanostatic discharge curve of the assembled pouch cell.

3. Anode Utilization

The anode utilization is calculated as:

$$U_n = Q_{cell} / C_{n,theo} \times 100\%$$

where U_n represents the percentage of the theoretical anode capacity that is effectively utilized in the full cell.

DFT calculations:

The present first principle DFT calculations are performed by Vienna Ab initio Simulation Package (VASP) [2] with the projector augmented wave (PAW) method [3]. The exchange-functional is treated using the generalized gradient approximation (GGA) of Perdew-Burke-Emzerhof (PBE) [4] functional. The energy cutoff for the plane wave basis expansion was set to 450 eV and the force on each atom less than 0.05 eV/Å was set for convergence criterion of geometry relaxation. Grimme's DFT-D3 methodology[5] was used to describe the dispersion interactions. Partial occupancies of the Kohn-Sham orbitals were allowed using the Gaussian smearing method and a width of 0.05 eV. The Brillourin zone was sampled with Gamma point 2× 2 × 1 through all the computational process. The self-consistent calculations apply a convergence energy threshold of 10^{-5} eV. A Climbing Image Nudged Elastic Band (CI-NEB) method was used to locate the transition states with the same convergence standard.

The free energy were calculated by the equation: $\Delta G = \Delta E_{DFT} + \Delta E_{ZPE} - T\Delta S$, where ΔE_{DFT} is the DFT electronic energy difference of each step, ΔE_{ZPE} and Δ_S are the correction of zero-point energy and the variation of entropy, respectively, which are obtained by vibration analysis, T is the temperature (T = 300 K).

Calculation of the effective magnetic moment and the number of unpaired electrons:

The effective magnetic moment (μ_{eff}) was determined by fitting the magnetic susceptibility (χ), which is defined as:

$$\chi = \frac{M}{H}$$

where M is the magnetization and H is the applied magnetic field.

The temperature-dependent magnetic susceptibility follows the Curie-Weiss law:

$$\chi = \frac{C}{T - \Theta}$$

where Θ is the Curie-Weiss temperature, T is the absolute temperature, and C is the Curie constant. The value of C was extracted from the linear fitting of the χ^{-1}-T plots shown in Fig. S28.

According to Langevin theory, the effective magnetic moment μ_{eff} can be calculated from the Curie constant using the following relation:

$$\mu_{eff} = \sqrt{8C}\mu_B$$

Here, μ_B is the Bohr magneton.

The number of unpaired electrons at the metal center can then be estimated from μ_{eff} using the spin-only expression:

$$\mu_{\text{eff}} = \sqrt{n(n+2)}\,\mu_{\text{B}}$$

where n denotes the number of unpaired electrons.

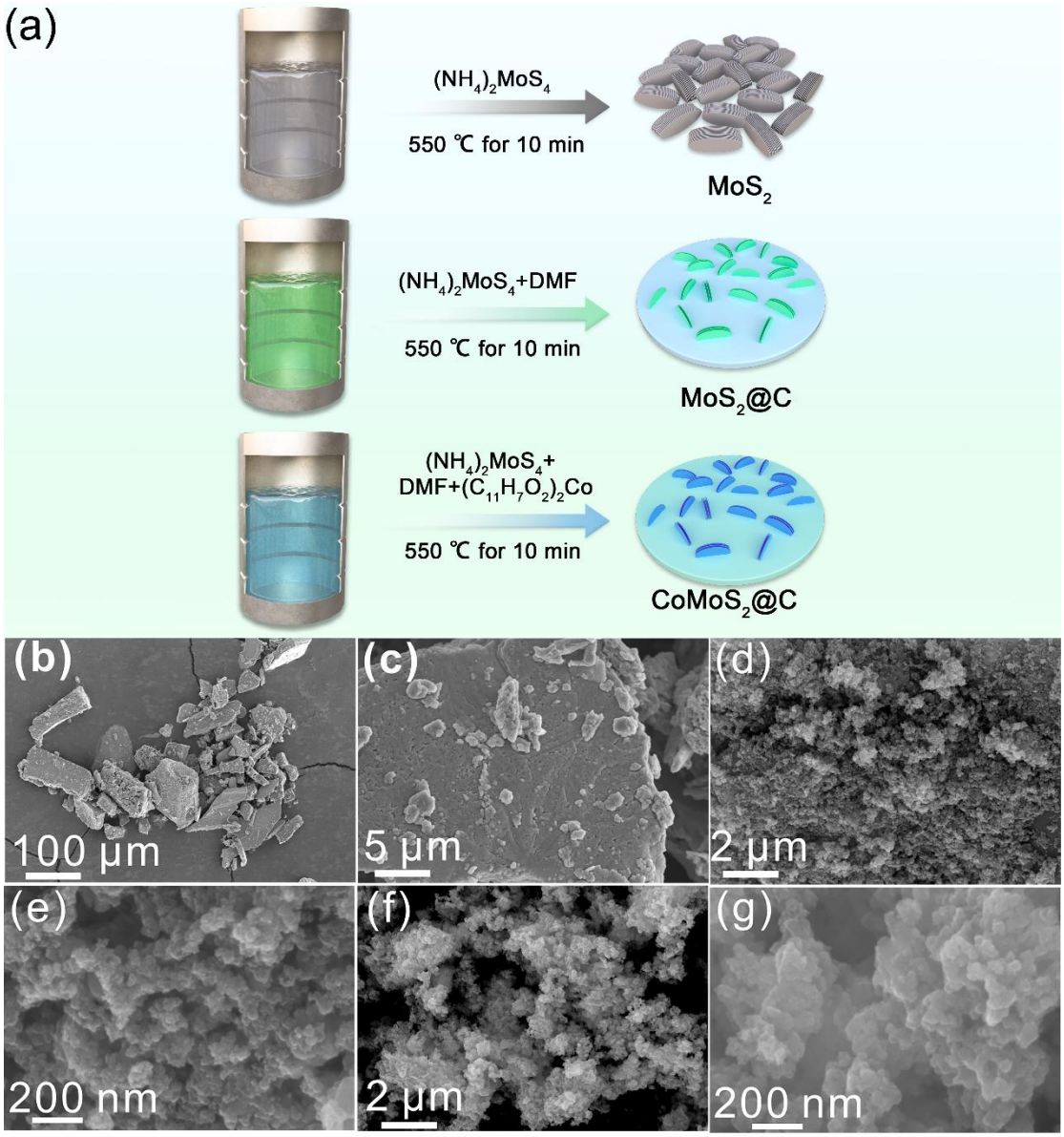

Fig. S1 (a) The fabrication diagram of MoS_2, MoS_2@C, and $CoMoS_2$@C. SEM images of (b, c) MoS_2, (d, e) MoS_2@C, and (f, g) $CoMoS_2$@C.

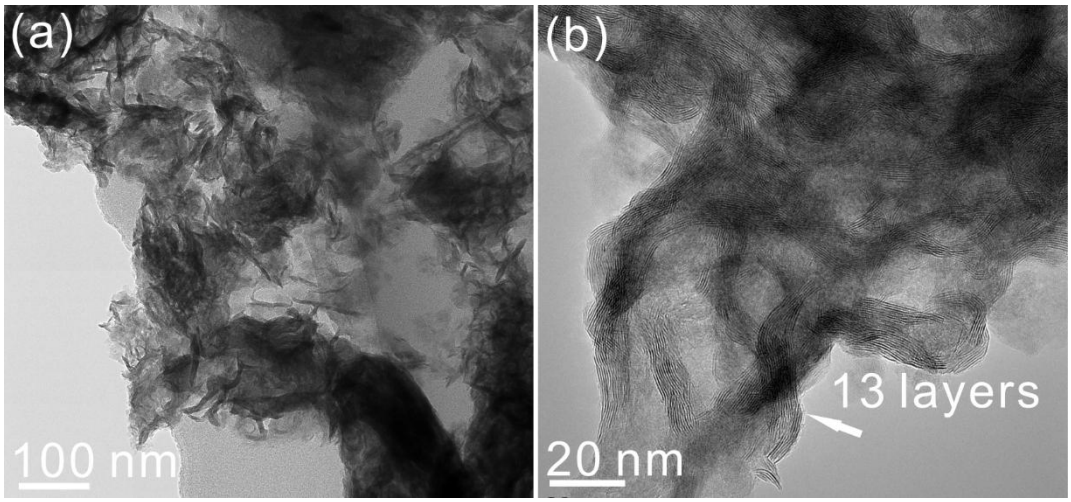

Fig. S2 (a) TEM and (b) HRTEM image of MoS_2.

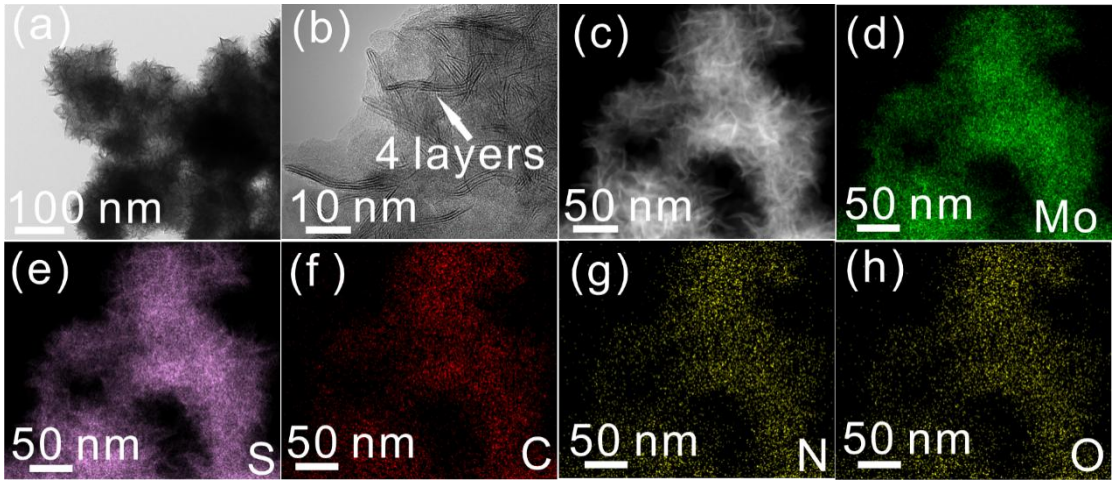

Fig. S3 (a) TEM, (b) HRTEM image, (c-h) EDS images of MoS_2@C.

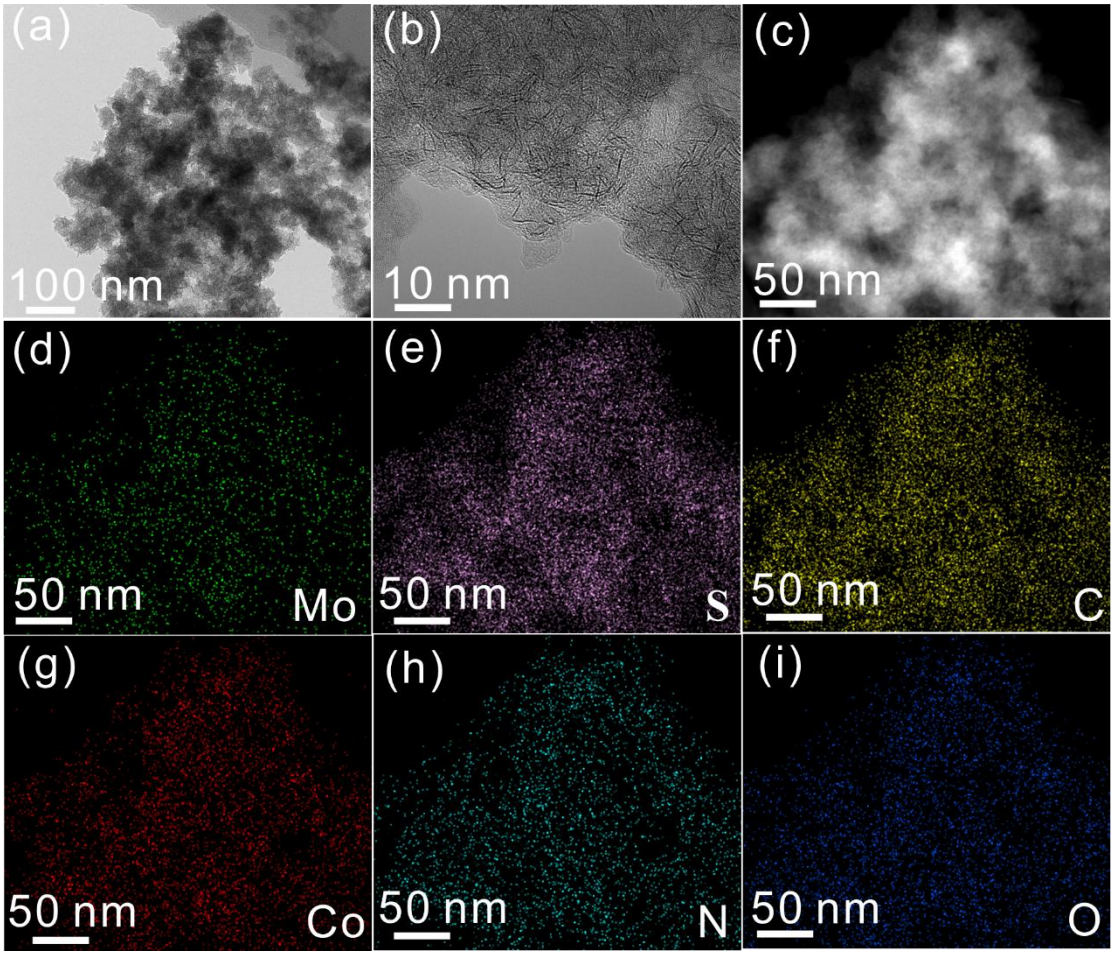

Fig. S4 (a) TEM, (b) HRTEM image, (c-i) EDS images of $CoMoS_2$@C.

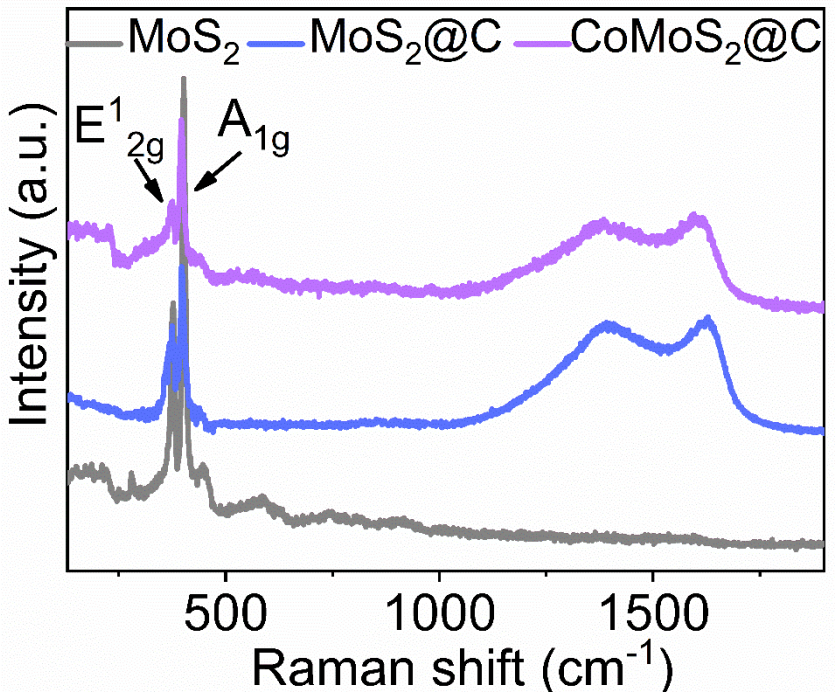

Fig. S5 Raman spectra of MoS_2, MoS_2@C, and $CoMoS_2$@C.

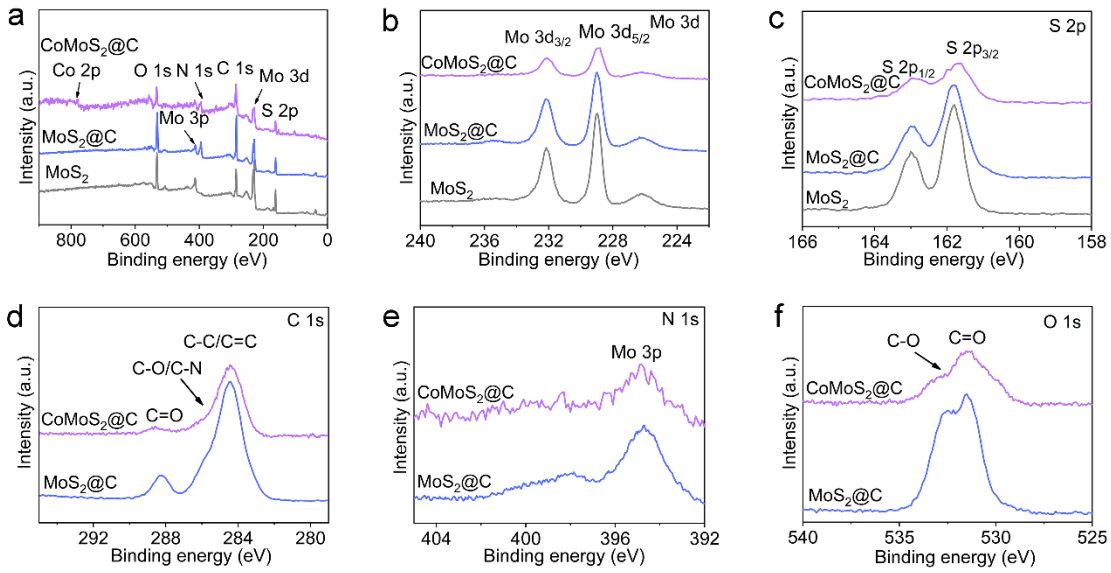

Fig. S6 (a) XPS survey peaks, high-resolution XPS spectra of (b) Mo 3d, and (c) S 2p of MoS_2, MoS_2@C, and $CoMoS_2$@C samples. High-resolution XPS spectra of (d) C 1s, (e) N 1s, and (f) O 1s of MoS_2@C and $CoMoS_2$@C samples.

Table S1 Fitting results of XPS spectra of all the samples.

Samples	Mo (at%)	S (at%)	Co (at%)	C (at%)	N (at%)	O (at%)
MoS_2	30.88	61.05	0	3.86	0	4.21
MoS_2@C	6.11	12.26	0	67.74	9.06	4.83
$CoMoS_2$@C	3.87	8.33	1.67	73.94	8.23	3.96

The doping amount of N elements in the carbon materials should be calculated by N (at%)/(C (at%)+N (at%)+O (at%))*100%, respectively. The doping amount of Co element in MoS_2 should be calculated by Co (at%)/(Co (at%)+Mo (at%)+S (at%))*100%. The specific doping amount is represented in Tables S1 and S2.

Table S2 The doping amount of Co element in MoS_2.

Samples	Co (at%)
$CoMoS_2$@C	12.04

Table S3 The doping amount of N and O elements in the carbon matrix.

Samples	N (at%)	O (at%)
MoS_2@C	11.10	5.92
$CoMoS_2$@C	9.56	4.60

Table S4 The elemental analysis (EA) results of the obtained samples.

Samples	Co (wt%)	Mo (wt%)	S (wt%)	C (wt%)	N (wt%)	O (wt%)
MoS_2@C	0	49.2	32.6	14.1	2.5	1.6
$CoMoS_2$@C	12.6	31.8	34.6	17.9	1.8	1.3

The S contents in the composites were measured using C/S elemental analyzers. The Co and Mo contents in the composites were tested by inductively coupled plasma mass spectrometer. The content of carbon matrix was calculated as a difference to 100 wt%. It can be seen that the mass percentages of carbon matrix are 18.2, and 21.0 wt%, corresponding to MoS_2@C and $CoMoS_2$@C, respectively. The results are generally consistent with the TGA analysis.

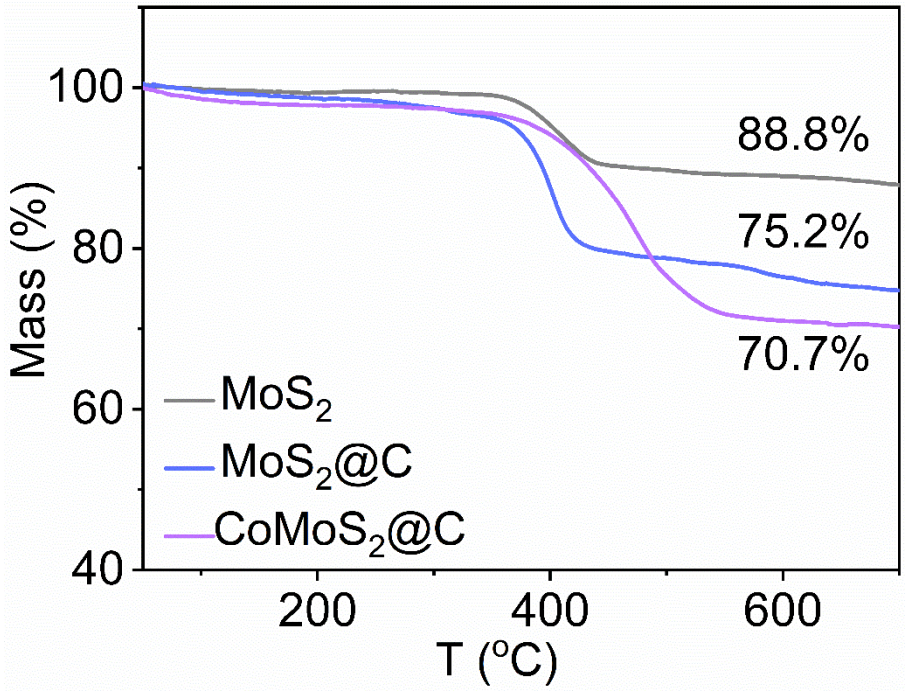

Fig. S7 TGA curves of MoS_2, MoS_2@C, and $CoMoS_2$@C samples.

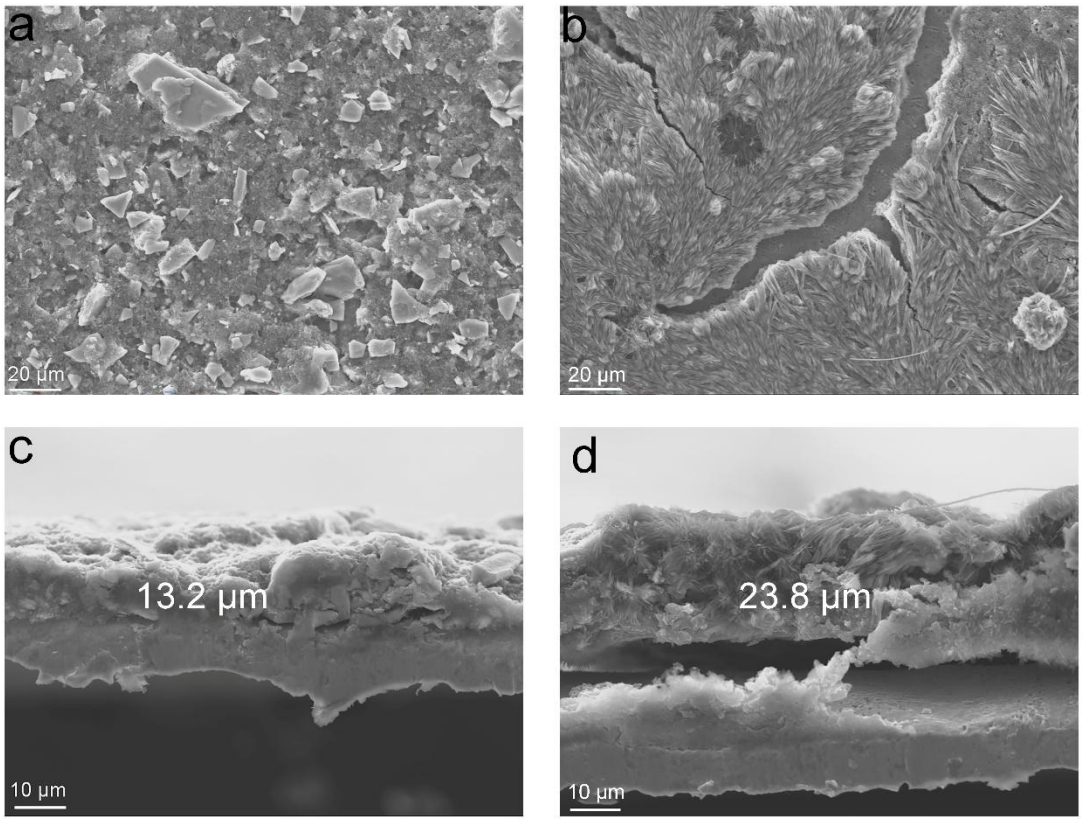

Fig. S8 Top-view morphology of MoS_2 electrode (a) before and (b) after 100 cycles. Cross-sectional morphology of MoS_2 electrode (c) before and (d) after 100 cycles.

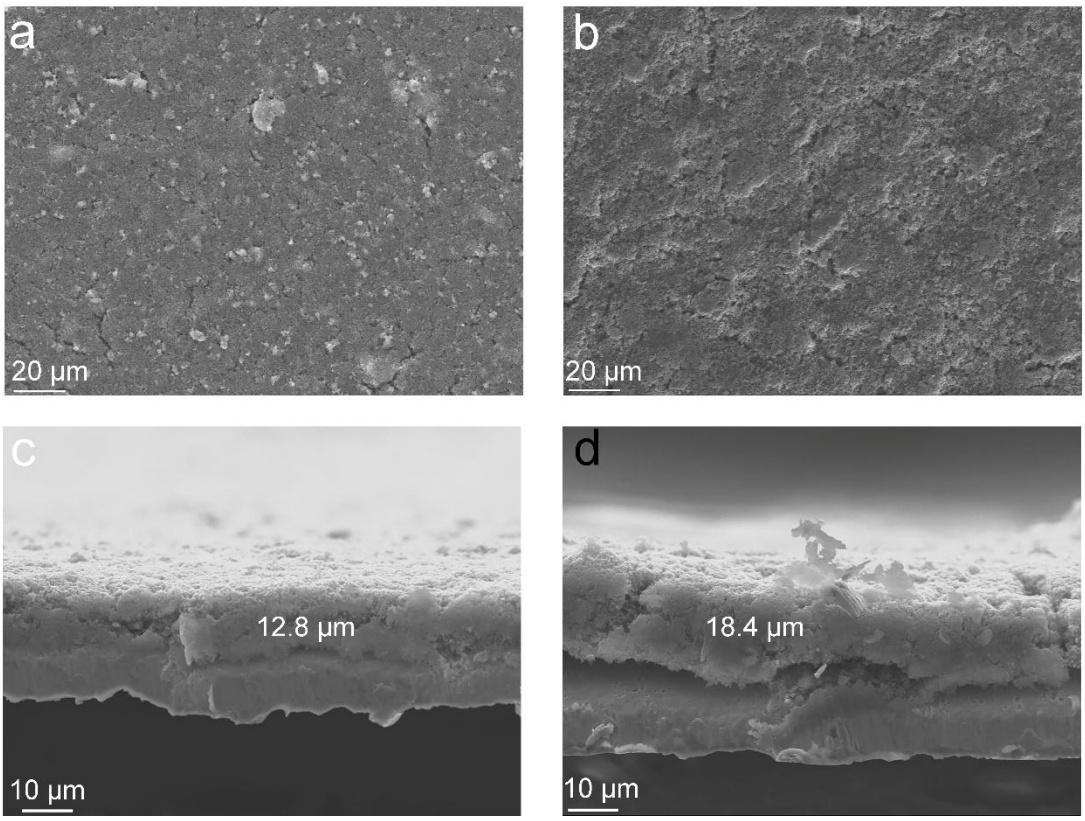

Fig. S9 Top-view morphology of MoS_2@C electrode (a) before and (b) after 100 cycles. Cross-sectional morphology of MoS_2@C electrode (c) before and (d) after 100 cycles.

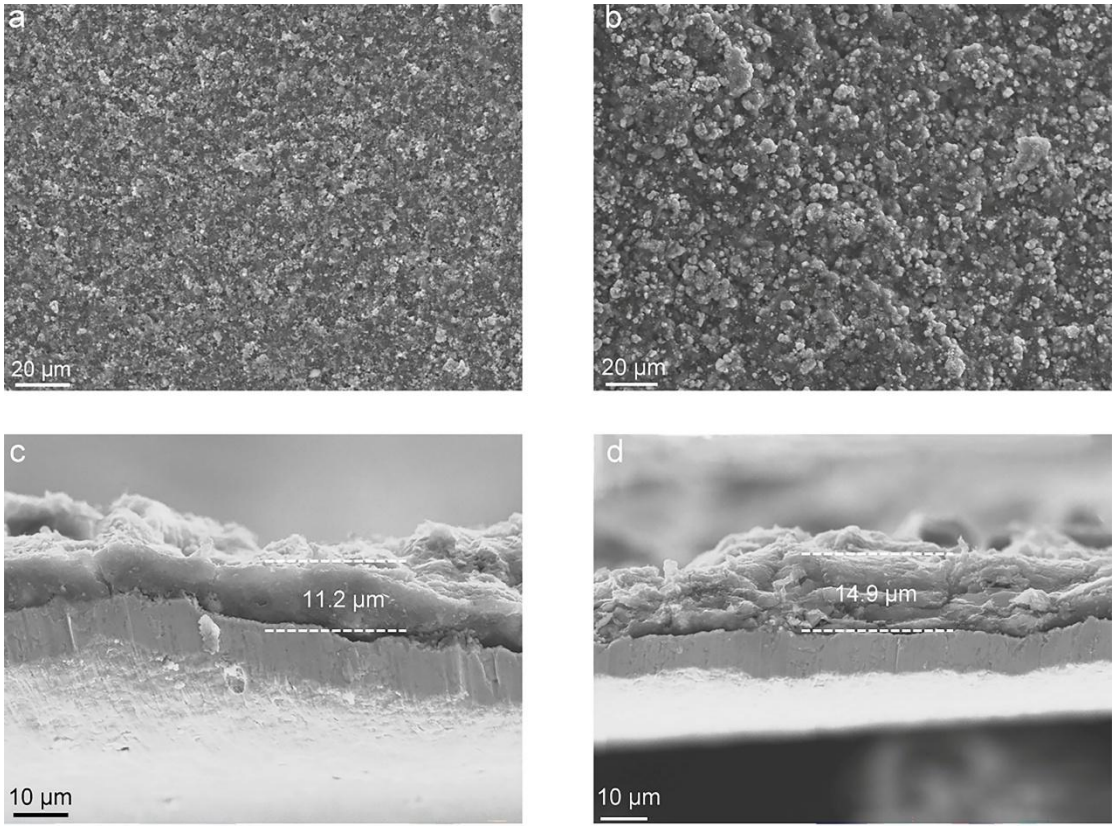

Fig. S10 Top-view morphology of $CoMoS_2$@C electrode (a) before and (b) after 100 cycles. Cross-sectional morphology of $CoMoS_2$@C electrode (c) before and (d) after 100 cycles.

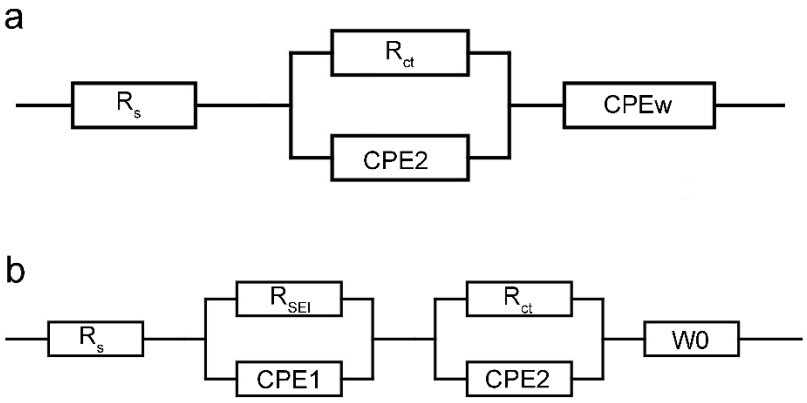

Fig. S11 The fitted circuits of EIS spectra in Figs. 2d and e. (a) before and (b) after rate tests.

Table S5 R_s, R_{ct}, R_{SEI}, and the slop of the sloping line of electrodes in low-frequency region before and after rate test. The data are from the fitted circuit of EIS spectra in the manuscript in Figs. 2d and e.

Samples	R_s	R_{ct}	R_{SEI}	slope
MoS_2, before rate test	4.3	247.5	0	1.0
MoS_2@C, before rate test	3.1	82.8	0	4.8
$CoMoS_2$@C, before rate test	2.2	64.4	0	9.6
MoS_2, after rate test	5.9	392.9	74.8	0.7
MoS_2@C, after rate test	3.7	113.2	26.5	1.8
$CoMoS_2$@C, after rate test	2.9	83.4	10.3	2.4

Table S6 Comparison of electrochemical performances of $CoMoS_2$@C with previously reported MoS_2-based anode materials for SIBs in open reports. C_C-charge capacity (mAh g^{-1}), C_R-capacity retention (%), M_L-mass loading (mg cm^{-2}), J-current density (A g^{-1}), N_C-cycle number, NA-not available.

Samples	C_C	C_R	M_L	J	N_C	References
$CoMoS_2$@C	**764.0**	**96.6**	**1.2**	**0.1**	**100**	**This work**
$CoMoS_2$@C	**552.8**	**85.4**	**1.2**	**5**	**3000**	**This work**
MoS_2@NC-SAMn/CNTs	284.1	89.9	NA	1	2000	Angew. Chem., Int. Ed. Engl. 2024, 63, e202411255.
L-MoS_{2-x}	636.02	93.4	NA	0.1	100	Advanced Science (2025): e17576
Fe-M-HoMS-Q	310.0	83.68	1.5	5	500	Angew. Chem., Int. Ed. Engl. 2024, 136, e202400285.
SMO-4	345	82.9	1.32	5	2300	Adv. Funct. Mater. 2024, 34, 2311471.
SA Co-MoS_2/C	604.0	NA	0.8-1.2	0.1	NA	Adv. Mater. 2023, 35, 2211690
SA Co-MoS_2/C	334.0	~86.8	0.8-1.2	5	1380	Adv. Mater. 2023, 35, 2211690
C-p-MoS_2/CNT	666.0	NA	1.2-1.5	0.05	NA	Adv. Funct. Mater. 2023, 33, 2207548
C-p-MoS_2/CNT	445	90.4	1.2-1.5	0.1	300	Adv. Funct. Mater. 2023, 33, 2207548
C-p-MoS_2/CNT	295	74.5	1.2-1.5	2.5	1500	Adv. Funct. Mater. 2023, 33, 2207548
1T-rich MoS_2/m-C	557	NA	1	0.1	80	ACS Nano 2022, 16,

						12425−12436
1T-rich MoS_2/m-C	364	NA	1	2	1000	ACS Nano 2022, 16, 12425−12436
Cu_2S@carbon@MoS_2	430	NA	NA	0.05	NA	Angew. Chem., Int. Ed. Engl. 2020, 59, 7178
Cu_2S@carbon@MoS_2	297	NA	NA	3	NA	Angew. Chem., Int. Ed. Engl. 2020, 59, 7178
Cu_2S@carbon@MoS_2	~280	80.4	NA	0.3	200	ACS Nano 2021, 15, 13814
ANDC/MoS_2	496	94.5	1.3	1	1000	ACS Nano 2021, 15, 13814
ANDC/MoS_2	336	72.4	1.3	5	300	ACS Nano 2021, 15, 13814
Nb_2CT_x@MoS_2@C	530	87.0	~1.1	0.1	200	ACS Nano 2021, 15, 7439
Nb_2CT_x@MoS_2@C	403	80	~1.1	1	2000	ACS Nano 2021, 15, 7439
N-MoS_2/C	401	77.9	1	0.13	200	Chem. Eng. J. 2020, 387, 124144
M-c MoS_2	401	89.1	NA	0.2	150	Nano Energy 2018, 51, 546

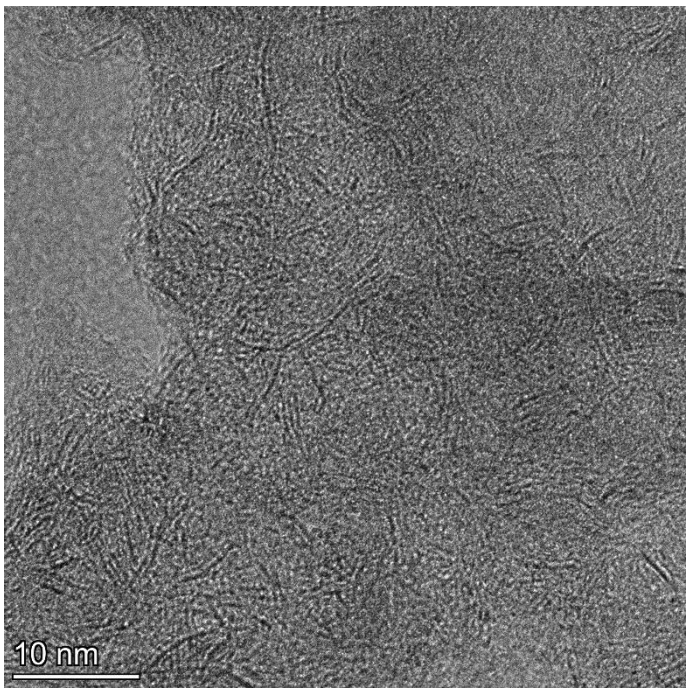

Fig. S12 HRTEM image of $CoMoS_2$@C after 18 s of electron-beam irradiation during *in situ* TEM measurements without applying a voltage.

To evaluate whether electron-beam irradiation could potentially affect the *in situ* TEM observations of the $CoMoS_2$@C sample, we conducted additional control experiments (Video S1), in which the sample was exposed solely to the electron beam without applying any bias voltage. During continuous observation for 18 s, no obvious structural changes indicative of electron beam-induced phase transitions was observed. This conclusion was further confirmed by post-irradiation HRTEM analysis, which showed that electron beam exposure did not induce detectable changes in the microstructure of $CoMoS_2$@C (Fig. S12).

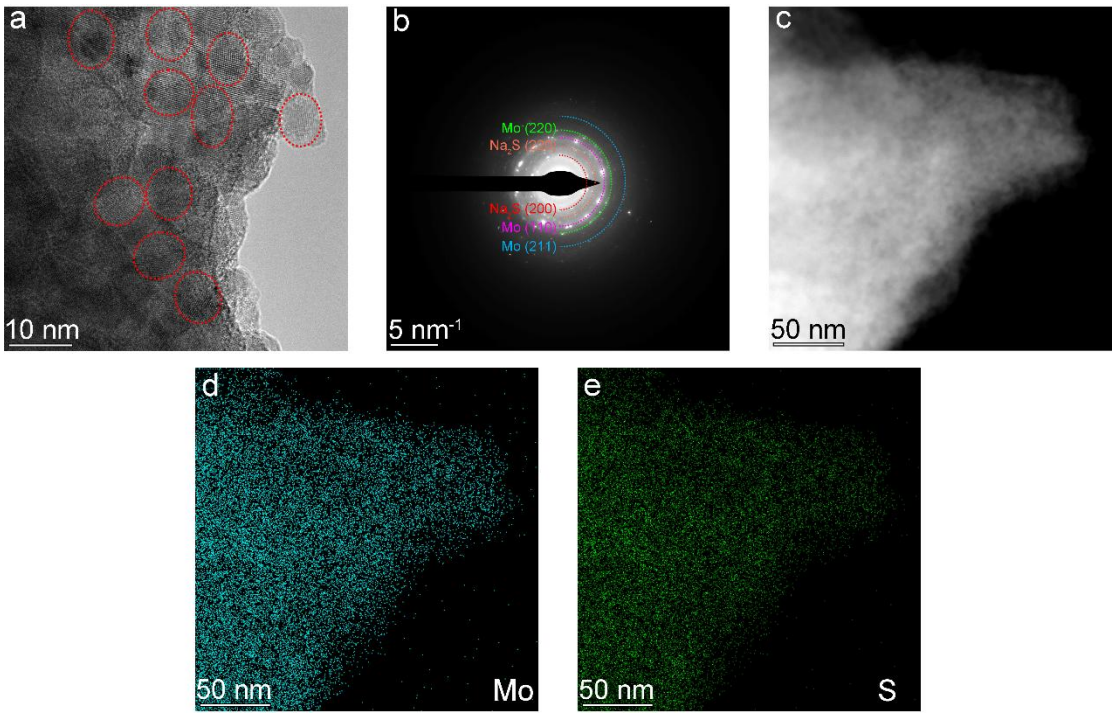

Fig. S13 (a) HRTEM image, (b) SAED pattern, and (c-e) EDS images of MoS_2 electrode after discharging to 0.01 V.

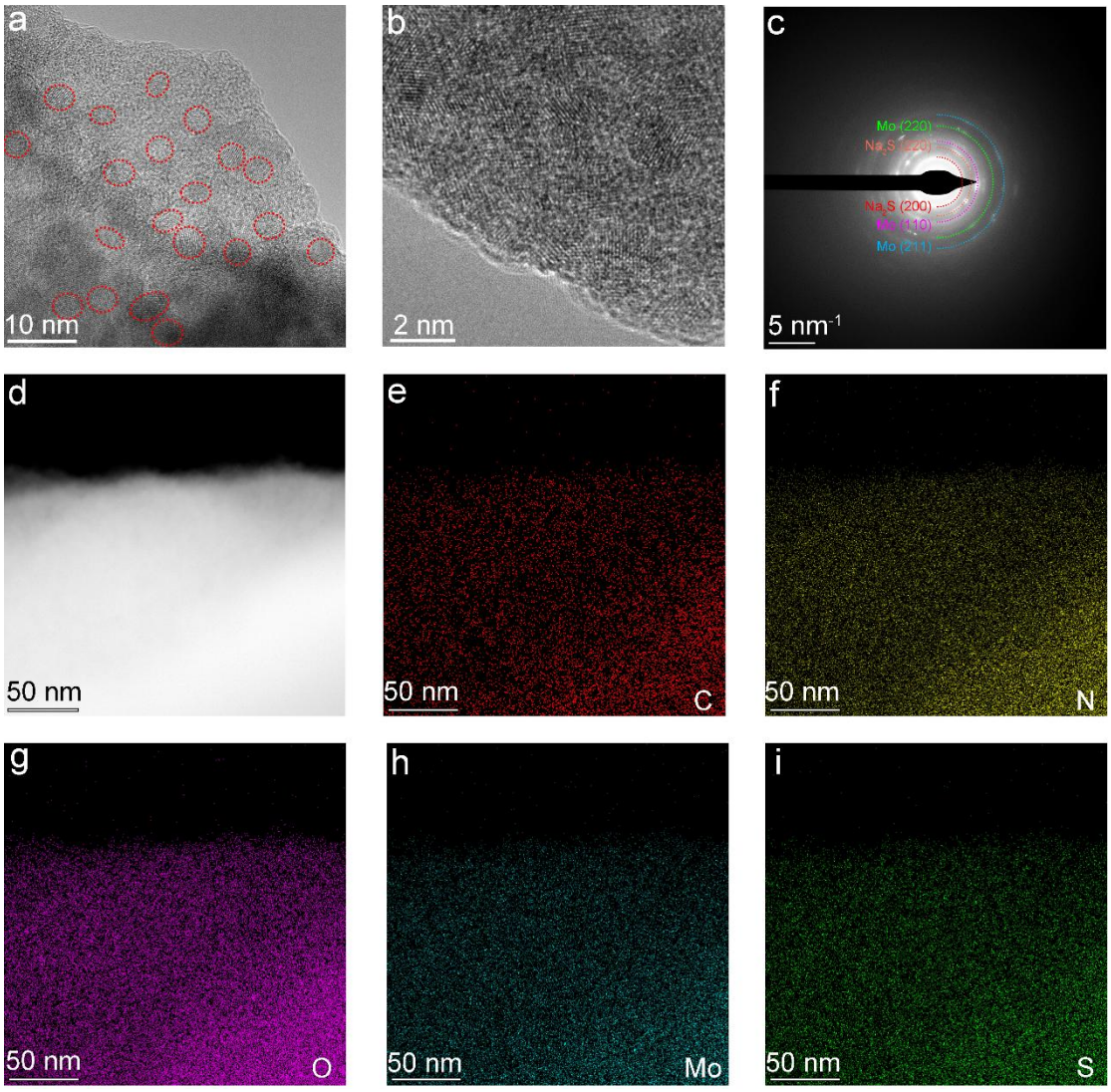

Fig. S14 (a, b) HRTEM images, (c) SAED pattern, and (d-i) EDS images of MoS_2@C electrode after discharging to 0.01 V.

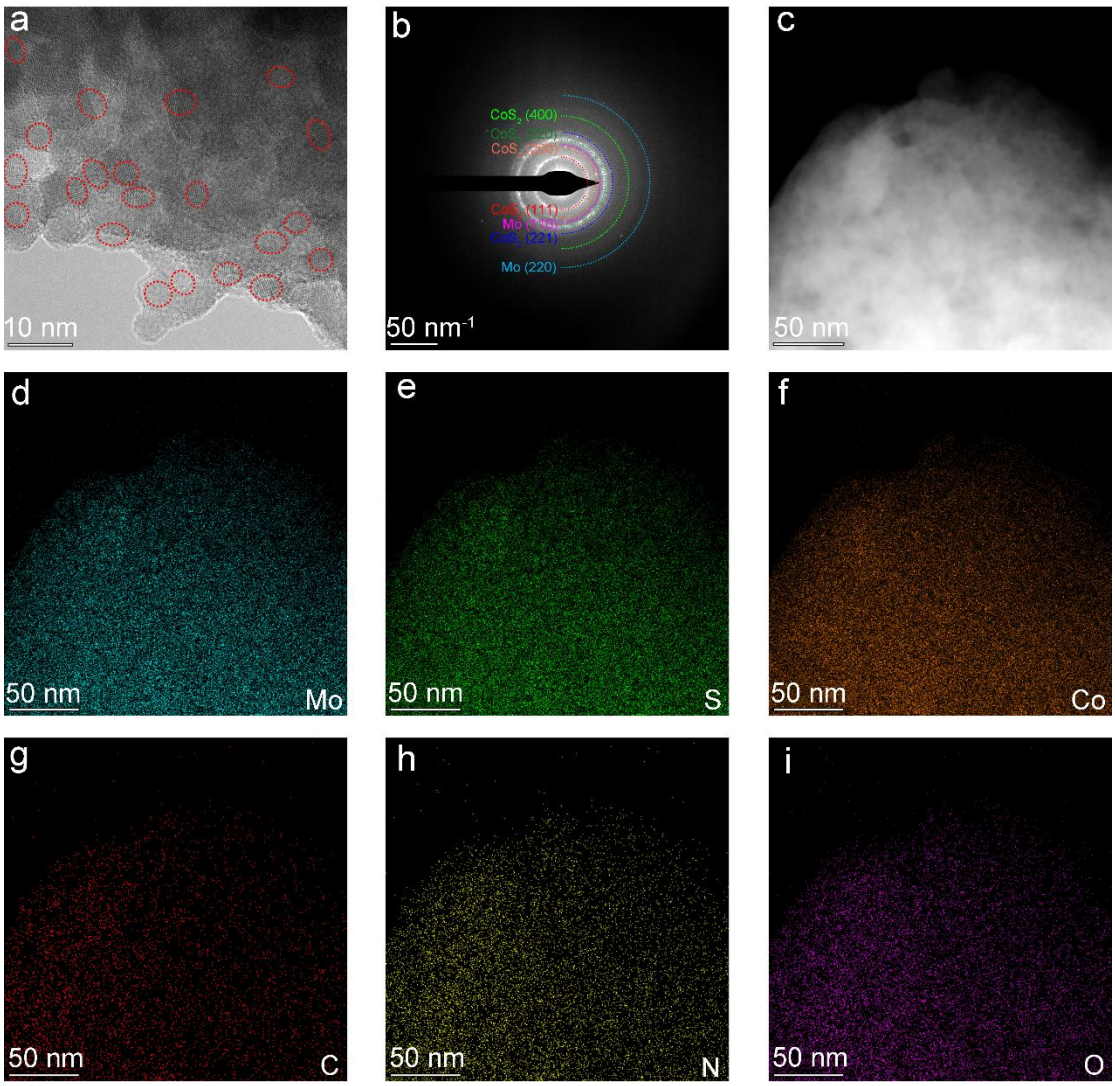

Fig. S15 (a) HRTEM images, (b) SAED pattern, and (c-i) EDS images of $CoMoS_2$@C electrode after charging to 3 V.

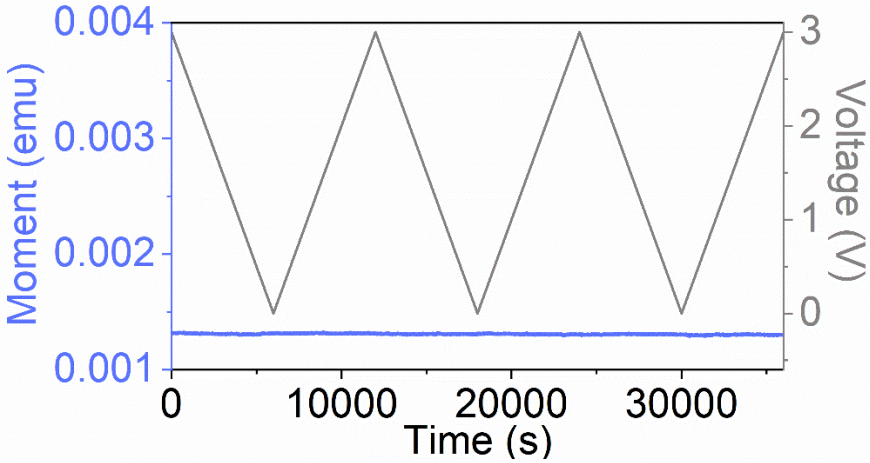

Fig. S16 *In situ* magnetometry of blank cell during electrochemical cycling.

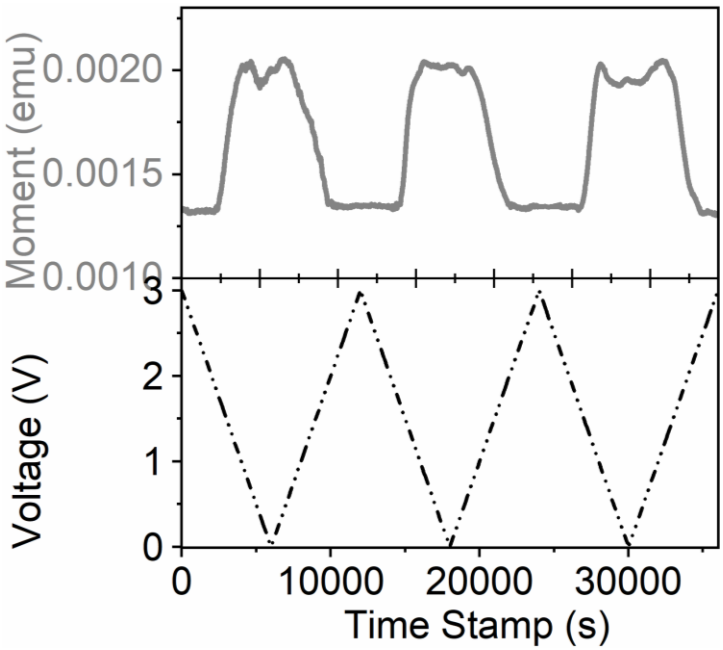

Fig. S17 Initial data of in situ magnetometry of $CoMoS_2$@C during electrochemical cycling.

To eliminate the influence of electrochemically inactive components in the assembled cells, including copper foil, electrolyte, binder, and conductive additives, on the *in situ* magnetic measurements, blank cells were assembled and subjected to identical in situ magnetic tests. Specifically, the blank cells were fabricated following the same procedure as that used for the in situ magnetic measurements, except that no active material was added, while all other components were kept unchanged. It should be noted that the *in situ* magnetic spectra shown in Fig. 3h were obtained by subtracting the magnetic response of the blank cell (Fig. S16) from the original in situ magnetic data (Fig. S17) and subsequently normalizing the results according to the Co content, thereby revealing the intrinsic magnetic behavior of the $CoMoS_2$@C electrode.

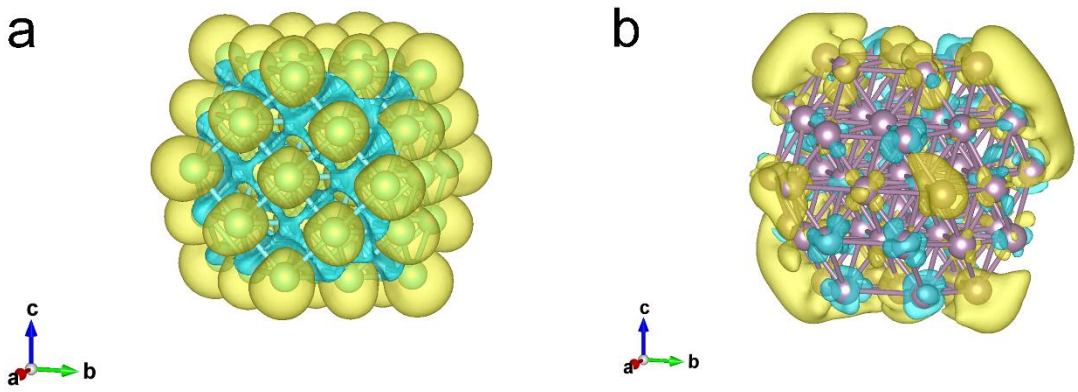

Fig. S18 Spin charge density distribution of (a) Co and (b) Mo clusters.

Table S7 Magnetic moments (μ_B) of individual atoms in the Co cluster in Fig. S18a obtained from DFT calculations.

1.187	1.547	1.546	1.545	1.731	1.732	1.731	1.803	1.546	1.73
1.73	1.731	1.802	1.73	1.546	1.731	1.73	1.546	1.546	1.733
1.803	1.73	1.729	1.801	1.732	1.802	1.729	1.729	1.547	1.731
1.546	1.73	1.547	1.803	1.73	1.731	1.731	1.547	1.546	1.731
1.729	1.801	1.731	1.73	1.73	1.802	1.732	1.803	1.731	1.802
1.73	1.731	1.73	1.802	1.802					

Table S8 Magnetic moments (μ_B) of individual atoms in the Mo cluster in Fig. S18b obtained from DFT calculations.

0.019	-0.066	-0.014	0.037	-0.004	-0.019	-0.053	0.088	-0.021	0.139
-0.082	0.126	-0.078	0.271	-0.055	-0.063	-0.004	-0.068	-0.017	-0.078
0.126	-0.043	0.15	0.073	0.066	0.007	0.227	0.126	0.075	-0.088
0.117	-0.087	-0.075	-0.082	0.081	-0.049	-0.108	0.032	-0.092	0.012
-0.041	0.128	0.125	-0.058	0.002	0.035	0.31	0.06	0.019	-0.005
0.181	0.142	0.061	-0.016	-0.064	0.049	0.241	0.035	0.191	

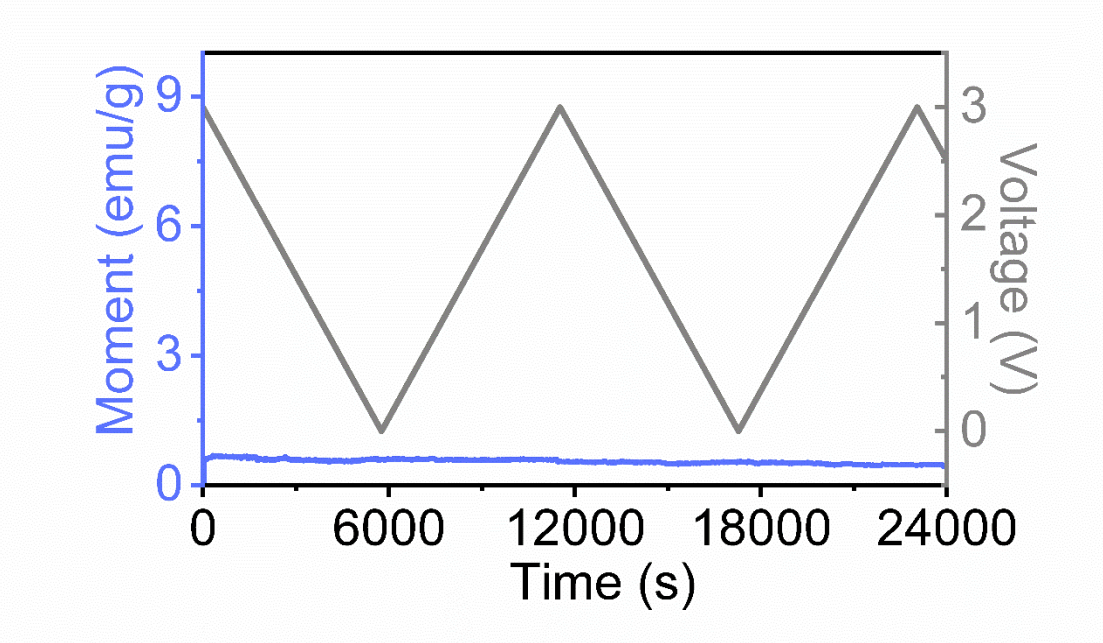

Fig. S19 *In situ* magnetometry of MoS_2 electrode during electrochemical cycling.

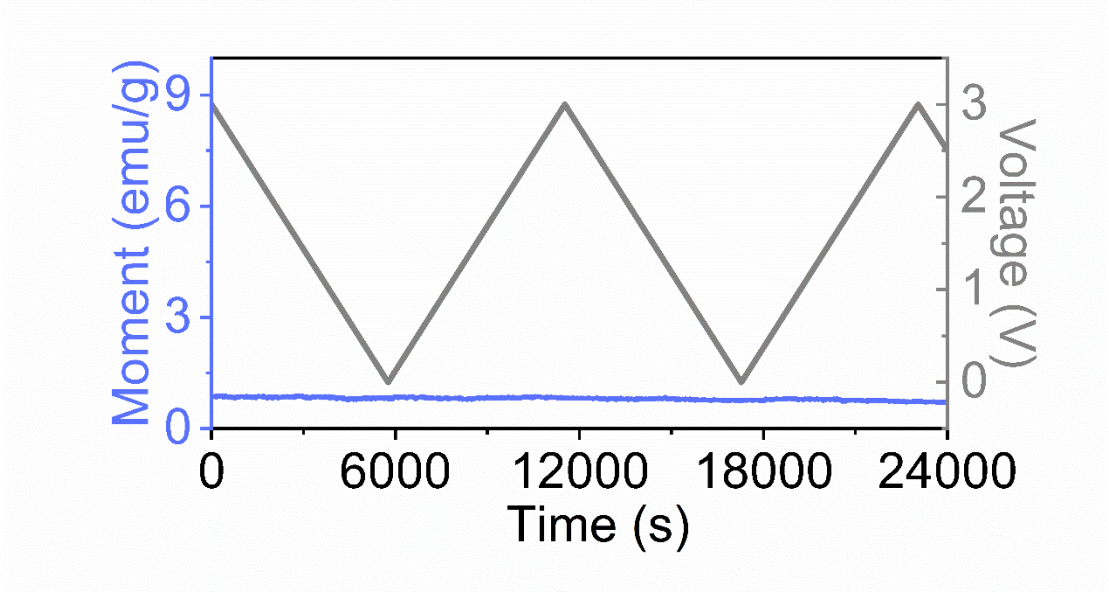

Fig. S20 *In situ* magnetometry of MoS_2@C electrode during electrochemical cycling.

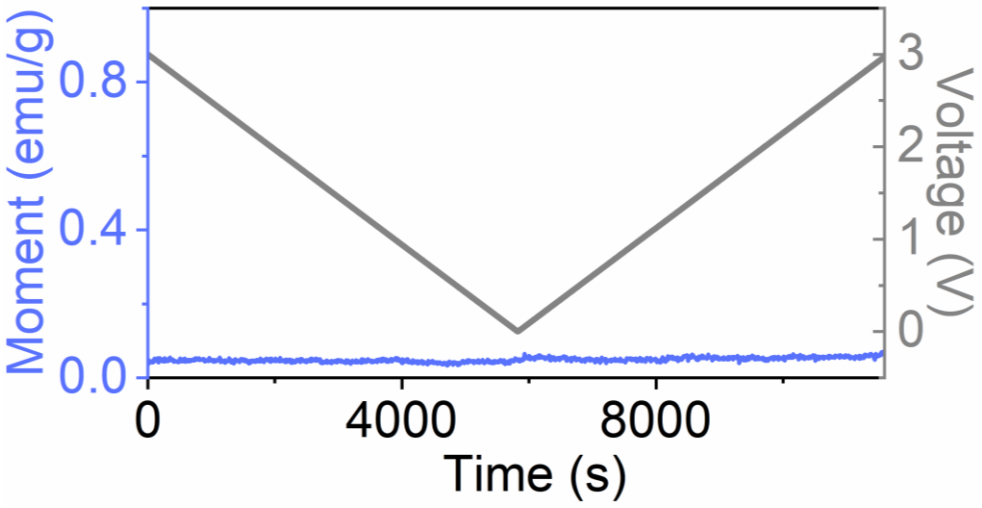

Fig. S21 *In situ* magnetometry of DMF-derived carbon electrode during electrochemical cycling.

We further performed in-situ magnetic measurements on DMF-derived carbon to clarify the origin of the magnetic response in $CoMoS_2$@C. The DMF-derived carbon was obtained by sealing DMF in a high-pressure autoclave inside a glovebox, followed by thermal treatment under the same conditions applied to the other samples.

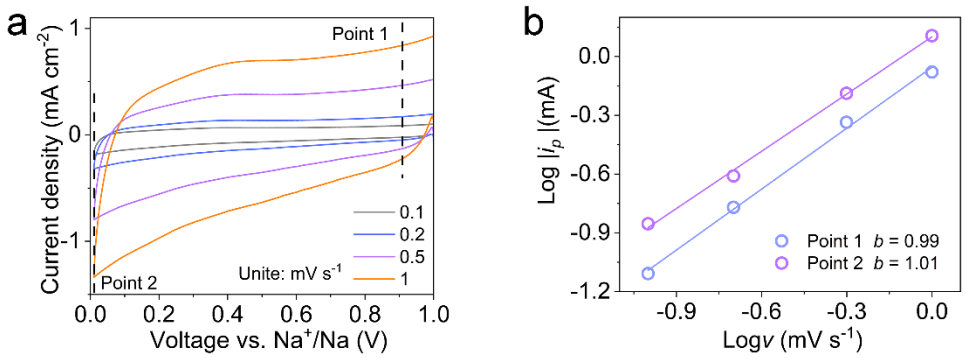

Fig. S22 (a) CV curves at the voltage range of 0.01-1 V and (b) log | i_p | against Log v at points 1 and 2 of $CoMoS_2$@C electrode.

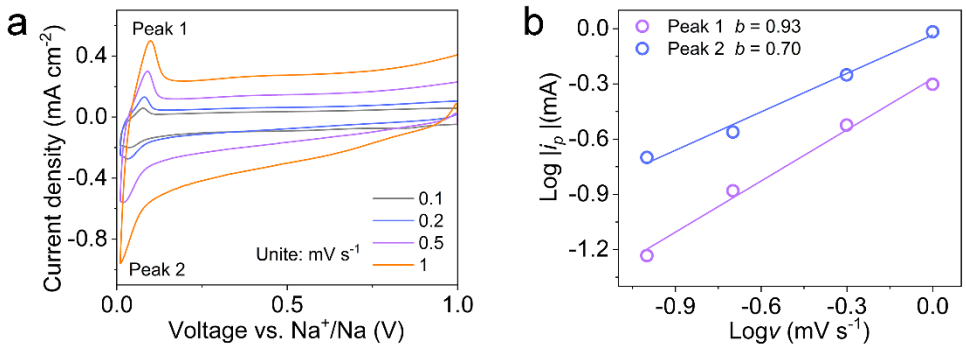

Fig. S23 (a) CV curves at the voltage range of 0.01-1 V and (b) log | i_p | against Log v at peaks 1 and 2 of MoS_2 electrode.

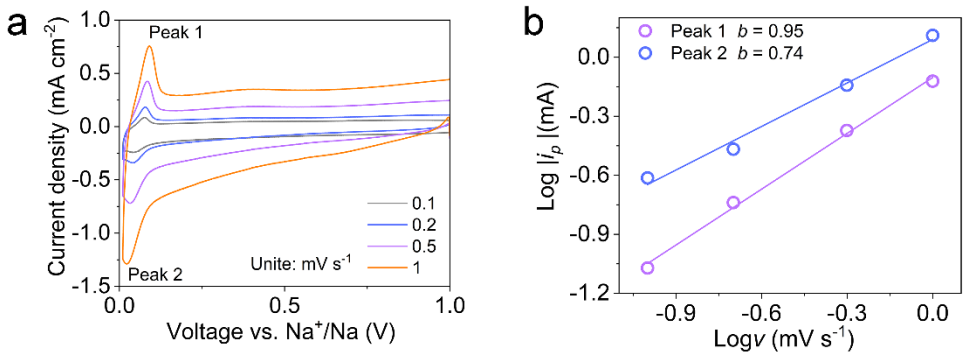

Fig. S24 (a) CV curves at the voltage range of 0.01-1 V and (b) log | i_p | against Log v at peaks 1 and 2 of MoS_2@C electrode.

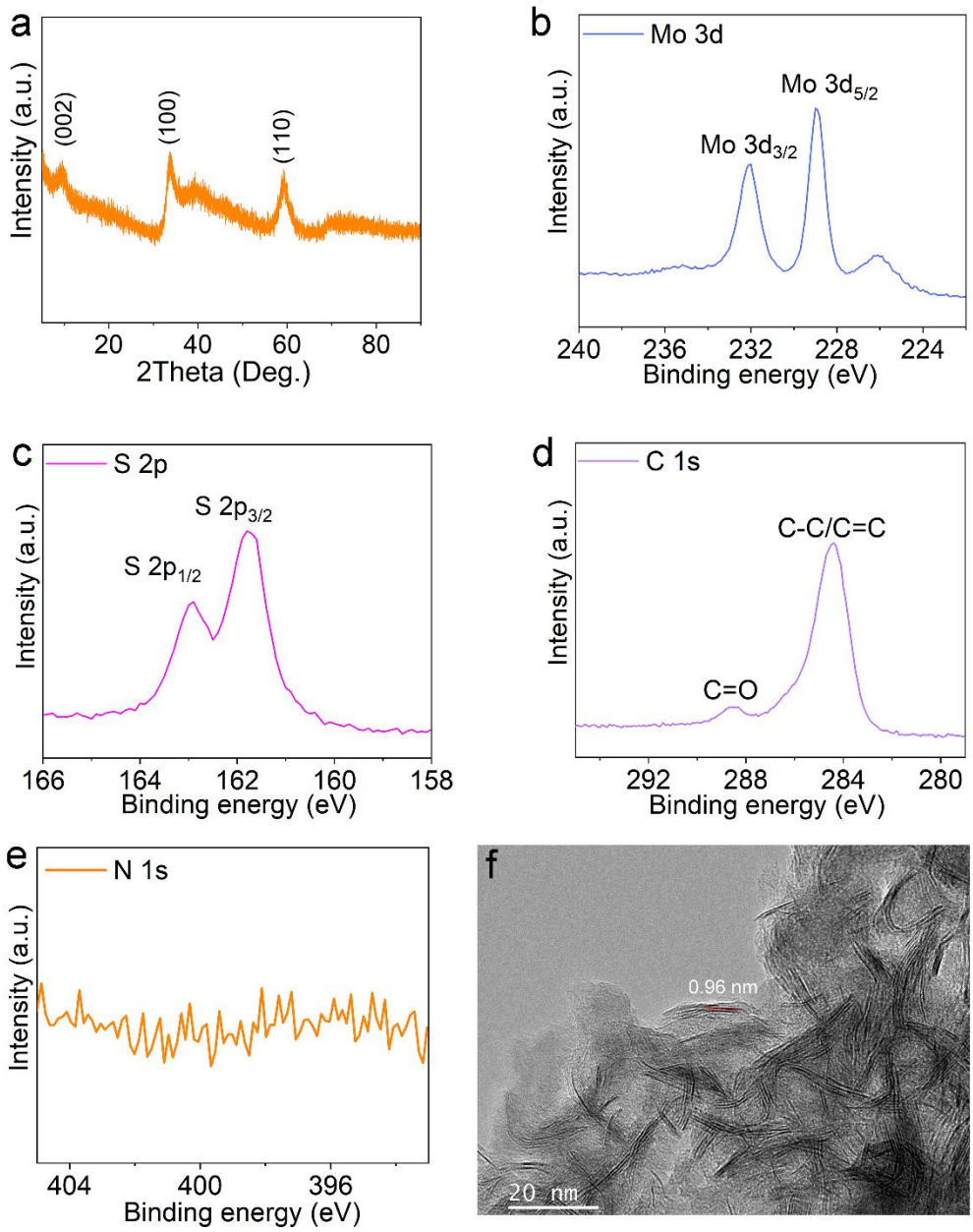

Fig. S25 (a) XRD pattern, high-resolution XPS spectra of (b) Mo 3d, (c) S 2p, (d) C 1s, and (e) N 1s of MoS_2@C-I sample without N doping. (f) HRTEM image of MoS_2@C-I sample without N doping.

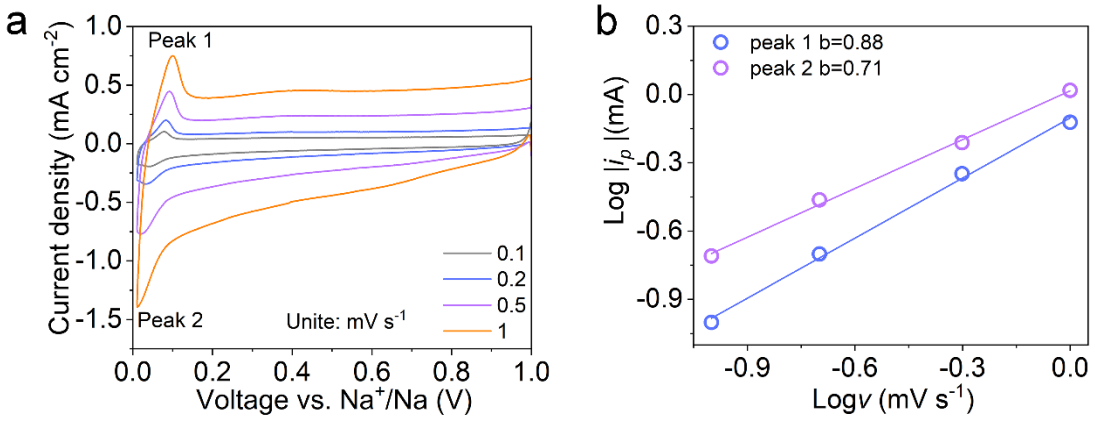

Fig. S26 (a) CV curves at the voltage range of 0.01-1 V and (b) log | i_p | against Log v at peaks 1 and 2 of the MoS_2@C-I electrode without N doping.

CV measurements in the 0.01-1 V window show nearly rectangular curves for $CoMoS_2$@C (Fig. S22a), with *b*-values close to 1 for all samples ($CoMoS_2$@C: 0.99, 1.01, Fig. S22b; MoS_2: 0.93, 0.70, Fig. S23; MoS_2@C: 0.95, 0.74, Fig. S24), indicating predominantly surface-controlled behavior. The slightly higher *b*-values of $CoMoS_2$@C reflect an enhancement of surface-controlled kinetics, consistent with the spin-polarized surface capacitance effect. To further rule out the influence of N doping on the *b*-values, dimethyl sulfoxide (DMSO) was used instead of DMF to dissolve $(NH_4)_2MoS_4$, while all other synthesis parameters were kept identical to those used for MoS_2@C, yielding the MoS_2@C-I sample without N doping. Comparison of the XRD, XPS, and HRTEM characterizations of MoS_2@C-I (Fig. S25) with those of MoS_2@C (Fig. 1c, 1e and Figs. S6b-S6e) shows that, apart from the absence of N doping in MoS_2@C-I (Fig. S25e), the crystal structure and phase composition of MoS_2@C-I are essentially identical to those of MoS_2@C. CV measurements of the MoS_2@C-I electrode in the 0.01-1 V voltage window (Fig. S26) indicate that the *b*-values corresponding to peak 1 and peak 2 are 0.88 and 0.71, respectively. Compared with the corresponding b-values of the MoS_2@C electrode, N doping leads to only a marginal increase in the *b*-value of MoS_2@C, and the enhancement is not pronounced. These results further confirm that the higher *b*-values observed for $CoMoS_2$@C relative to MoS_2@C do not originate from N doping. Importantly, *b*-values alone cannot fully

capture the contribution of spin-polarized electrons, as they are relatively insensitive to localized interfacial effects or electronic structure modulation. Complementary analyses, such as spin charge density calculations (Fig. S18 and Tables S7 and S8), EPR (Fig. 4d), and temperature-dependent magnetic susceptibility measurements (Fig. 4e), provide compelling evidence that Co^0-induced spin polarization facilitates interfacial Na^+ storage.

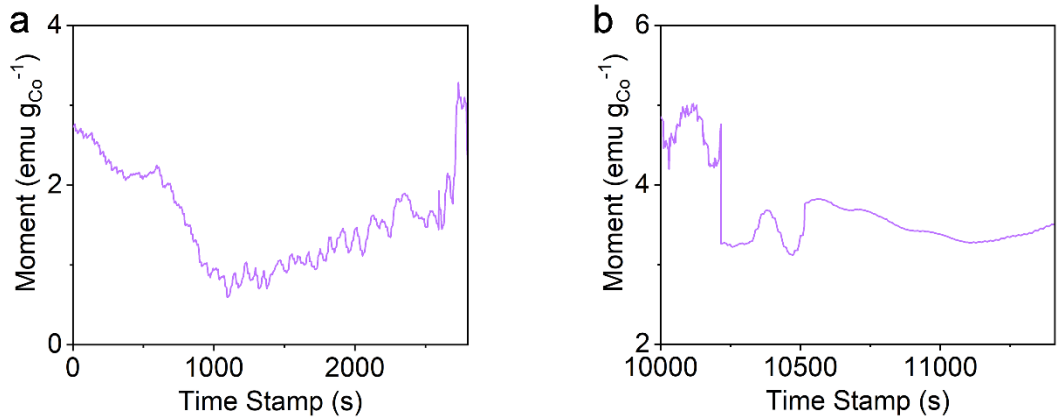

Fig. S27 Enlarged view of the magnetic response data corresponding to the (a) black and (b) blue dashed circles in Fig. 3h.

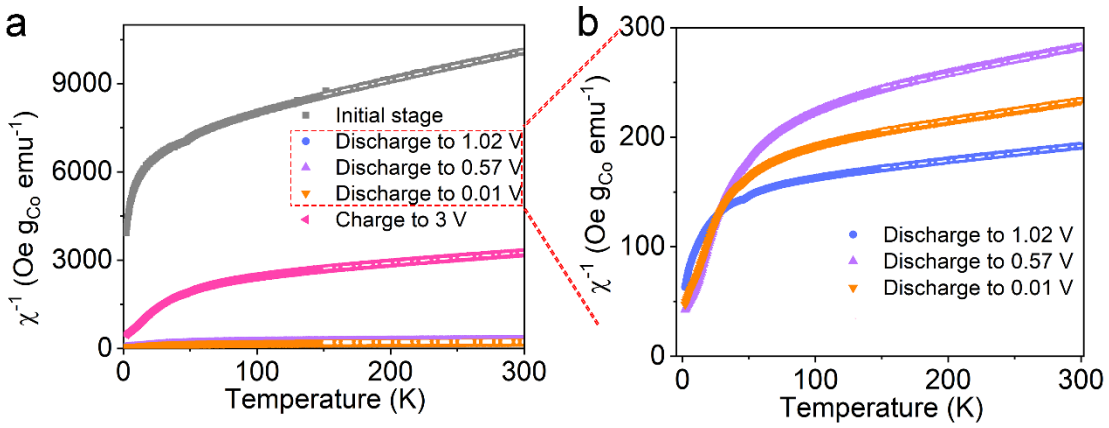

Fig. S28 (a) Temperature dependence inverse magnetic susceptibilities of $CoMoS_2$@C electrode at different electrochemical potentials. (b) The enlarged view of temperature dependence inverse magnetic susceptibilities at different potentials in the red box in Fig. S28(a).

Table S9 The obtained Curie constant (C), effective magnetic moment (μ_{eff}), and the number of unpaired d electrons (*n*).

Voltage	C	μ_{eff} (μ_B)	n
Initial stage	0.101	0.90	0.4
Discharge to 1.02 V	7.300	7.65	6.7
Discharge to 0.57 V	3.946	5.62	4.7
Discharge to 0.01 V	5.363	6.56	5.6
Charge to 3 V	0.275	1.48	0.8

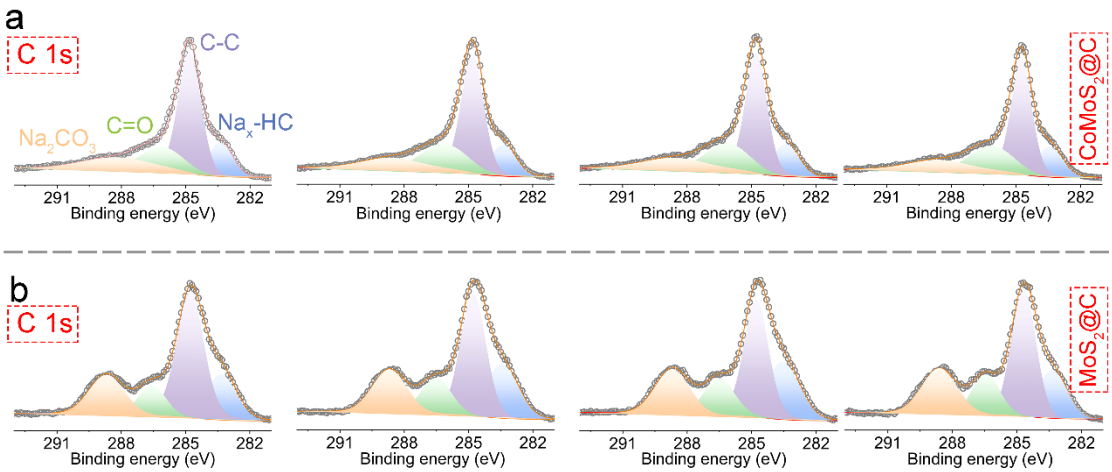

Fig. S29 C 1s spectra and corresponding depth profiling results of SEI formed in (a) $CoMoS_2$@C and (b) MoS_2@C electrode.

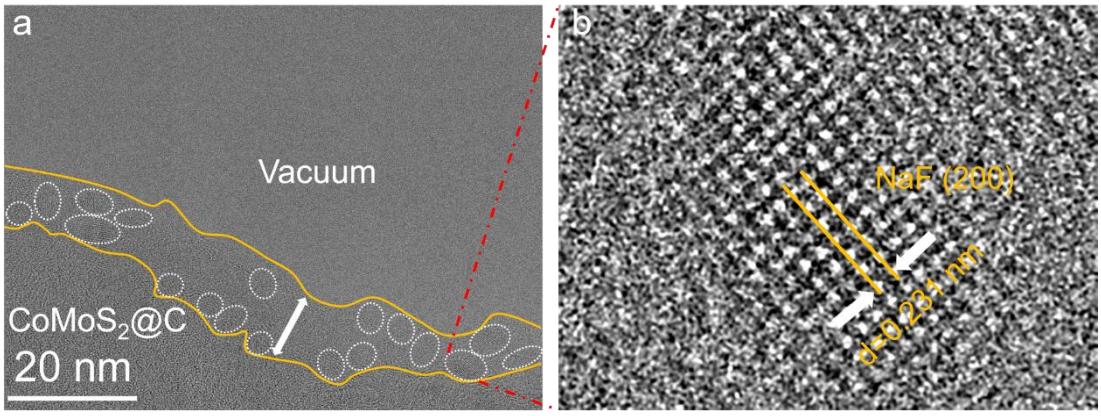

Fig. S30 (a) Cryo-TEM images of SEI layers of the $CoMoS_2$@C electrode and (b) the corresponding magnified view of the selected region in (a).

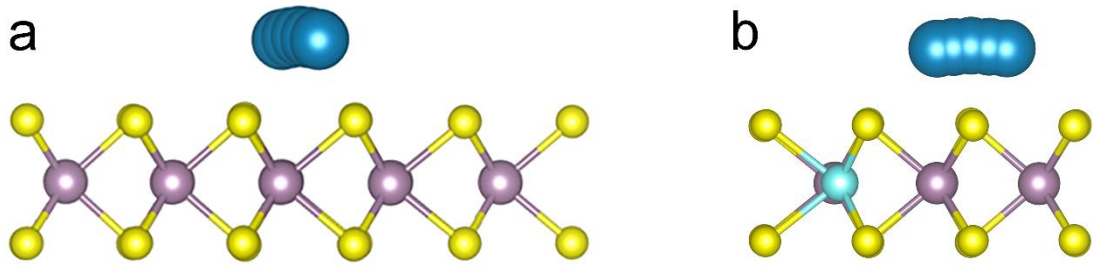

Fig. S31 Configurations of Na diffused in (a) monolayer MoS_2 and (b) Co-doped monolayer MoS_2.

References

[1] Tang, Jialiang, Daniel Kyungbin Kye, and Vilas G. Pol. J. Power Sources 2018, 396, 476-482.

[2] Kresse, G.; Furthmüller, J. Comp Mater Sci 1996, 6, (1), 15-50.

[3] Blöchl, P. E. Phys. Rev. B 1994, 50, (24), 17953-17979.

[4] Perdew, J. P.; Chevary, J. A.; Vosko, S. H.; Jackson, K. A.; Pederson, M. R.; Singh, D. J.; Fiolhais, C. Phys. Rev. B 1992, 46, (11), 6671-6687.

[5] Grimme, S.; Antony, J.; Ehrlich, S.; Krieg, H. J. Chem. Phys. 2010, 132, 154104.